Rayleigh-Bénard convection in a dielectric fluid under an external electric field with a melting boundary

Cai-Lei Lu,[1] Kang Luo,[1,*] Pu-Cheng Zhou,[2] and Hong-Liang Yi[1,*]
[1]*School of Energy Science and Engineering, and Key Laboratory of Aerospace Thermophysics, Harbin Institute of Technology, Harbin 150001, People's Republic of China*
[2]*Department of Information Engineering, PLA Army Academy of Artillery and Air Defense, Hefei 230031, People's Republic of China*

(Received 7 April 2021; accepted 3 June 2021; published 28 June 2021)

We perform a numerical analysis of Rayleigh-Bénard convection during solid-liquid phase change in the presence of an electric field. The objective is to examine the effects of the melting boundary and the electric field on the onset of flow motion and pattern formation. We characterize the timescale separation between the dynamics of the flow and that of the interface, which is dependent on the Rayleigh number Ra, the Prandtl number Pr, the Stefan number St, and the Fourier number Fo. It is found that (i) the delay of onset is a notable feature of the systems exhibiting phase transitions and convective instability compared to the traditional Rayleigh-Bénard convection; (ii) in the absence of the electric field, the critical Rayleigh number decreases monotonically with the timescale separation; (iii) in the presence of the electric field, the critical Rayleigh number can be lower than the classical value of $\mathrm{Ra}_c = 1707.76$. For moderate Rayleigh number ($\mathrm{Ra} = 10^5$), we predict the robust "locked-in" effect of the topography on convection. When the electric field is strong enough, this locked-in pattern will be broken and the system will evolve to a strong nonlinear regime in an inherently time-dependent fashion.

DOI: 10.1103/PhysRevFluids.6.063504

I. INTRODUCTION

Rayleigh-Bénard convection is one of the main heat transfer mechanisms in the natural sciences and engineering processes, responsible for most of the dynamics of the atmosphere and ocean [1], mantle formation [2], and the freezing or melting of material [3]. The two-way coupling between a flow and an evolving boundary, be it due to melting or solidification, has recently received much attention [4–8], because it is more relevant to the realistic natural configurations compared to the idealized systems with horizontal surfaces being generally considered as subjected to no-slip or free-slip boundary conditions. Focuses of flows over phase-change boundaries can be grouped into the following two categories: morphological instability, which focuses on the influence of flow on the topography's evolution and stability, and buoyancy-driven instability, which focuses on the hydrodynamic stability with horizontal boundary subjected to a phase-change condition.

Some of the studies to investigate the effects of flow on the stability of a solid-liquid interface are those of Refs. [6,9,10]. Davis *et al.* [9] studied the systems in which thermal convection and corrugations of a freezing interface are strongly coupled; they identified the pattern of convective flow and interfacial corrugation, and determined the parametric ranges in which different patterns occur. Toppaladoddi and Wettlaufer [6] studied the effects of externally imposed shear and buoyancy-driven flow on the stability of a solid-liquid interface. With a linear stability analysis

*Corresponding authors: luokang@hit.edu.cn; yihongliang@hit.edu.cn

they found that the buoyancy is the only destabilizing factor and that the shear flow stabilizes the system by inhibiting vertical motions and hence the upward heat flux. Sugawara *et al.* [10] experimentally investigated the double diffusive convection of a 20 wt % calcium chloride aqueous solution with horizontal ice plate melting from above. They detected the cellular polygonal patterns of the phase-change interface, which has also been observed by Esfahani *et al.* [4] by means of numerical simulations.

For Rayleigh-Bénard instability with a melting boundary, stabilities criteria based on nonlinear asymptotic analysis have been given for small Stefan number limit by Vasil and Proctor [11]. It is found that, compared to the classical Rayleigh-Bénard problem, the convection threshold can be modified and a morphological mode grows as soon as $\mathrm{Ra} = 1295.78$ is exceeded. The authors have also analyzed the complex locked-in spatially inhomogeneous pattern and shown that it is not so much a consequence of the nonautonomous nature of the dynamical system, but rather of the presence of the feedback from the Stefan condition, i.e., the melting top boundary. Considering the finite Stefan number, it is found that the delay of the onset of convection is one particularly notable feature when the presence of topography is included, as compared to the classical Rayleigh-Bénard system [4,7,12].

In addition to nontrivial topography dynamically generated by thermal convection, the modulation of wall temperatures [13], the magnetic field [14], and the direct current (DC) electric field [15] are also found to change the nature of convection both close to onset and in the supercritical regime. Of particular interest to the present study is the effect of electric field on the stability of thermal convection in a horizontal layer of fluid heated from below and with a melting top boundary. Over the last several decades the combined effects of an electric field and a thermal gradient on insulating liquids has been of great interest not only because of the interdisciplinary nature of such an interaction but also because of the potential technological advantages that may result from them [15–20]. Particularly, regarding a DC electric field, McCluskey *et al.* [18] gave experimental results that demonstrate that electroconvection induced by unipolar injection increases heat transfer, and that in certain circumstances, the convective heat transfer can be 10 times or more than that without electric field. For a complete overview of the canonical problem see literature reviews by Laohalertdecha *et al.* [21] and Rashidi *et al.* [22].

Compared to the well studied electrothermoconvection problem in single phase dielectric liquid [15–18,20], few studies concern the influences of an external electric field on Rayleigh-Bénard convection during the melting process. The works of Nakhla *et al.* [23,24] are a good start on the intertwined nature of Stefan systems and electroconvective flow. One of the experimental studies was designed to eliminate natural convection and to ensure conduction dominated the melting environment to isolate the influence of the electric field [23]. A new phenomenon, the solid extraction, was observed where the solid dendrites within the mushy zone were extracted toward the liquid bulk due to the application of EHD (nonuniform electric field). It is well known that the EHD body forces acting on a dielectric fluid could be expressed as [25]

$$\mathbf{f} = q\mathbf{E} - \frac{1}{2}E^2\nabla\varepsilon + \frac{1}{2}\left[\rho E^2\left(\frac{\partial\varepsilon}{\partial\rho}\right)_\theta\right]. \tag{1}$$

The three terms on the right-hand side of Eq. (1) represent the Coulomb force, the dielectric force, and the electrostrictive force, respectively. The later experiment with *n*-octadecane as phase-change material (PCM) indicates that Coulomb force, instead of dielectric force or electrostrictive force, is responsible for the main mechanism of heat transfer enhancement [24]. Specifically, the high voltage electrodes produce free ions in the dielectric liquid around the electrode of the same polarity, which in turn induces a jetlike structure initiated from the electrodes and moving toward the grounded electrode, thus impinging on the solid-liquid interface. This act of jet impingement leads to the high heat transfer enhancement in the regions around the electrodes.

Following the works of Nakhla *et al.* [23,24], Luo *et al.* [26] developed a numerical model based on the lattice Boltzmann method (LBM) to simulate the melting in the presence of EHD in a square

cavity; they found three kinds of instabilities arising during melting, corresponding to the small perturbation at the initial stage, the oscillation associated with the evolution of circulation cells, and the electroconvective instability in high driving parameters. Furthermore, by neglecting the effects of buoyancy in the bulk melt, Luo *et al.* [27] investigated the effects of a fixed solid-liquid interface on the stability of electroconvection in the liquid zone. They found that the solid phase over the interface results in a useless voltage drop in the solid phase which increases the linear and nonlinear stability threshold, although under these conditions the bifurcation of electroconvection is still of subcritical type. Recently this study was extended by He *et al.* [28] to investigate the effects of a conducting solid wall on the stability of electrothermoconvection, again using the lattice Boltzmann method. It was found that (i) both the linear stability criterion and the finite-amplitude stability criterion obtained for electrothermoconvection with a solid wall are higher than the corresponding values without a solid wall; (ii) increasing the electric Rayleigh number leads to the system passing from a steady state to an irregular unsteady one and then a reentrant stable state may arise; (iii) for a sufficiently strong electric field, the flow shows a chaotic feature.

One crucial point that Luo *et al.* [26,27] and He *et al.* [28] evidently overlooked is that because phase change occurs at boundaries, the convection melting system is intrinsically nonstationary, which leads to the complex interaction between the flow in the melt and the topography. Indeed, the topography of the top surface can affect the flow by creating flow patterns and coherent thermal structure that can differ from those occurring between flat plates or plates with prescribed roughness [4]. In addition, the complex coupling between solid and flow results in the evolution of topography that tends to produce stereotyped forms, and this morphology offers important clues to the history of a landscape and its development [29]. Here, motivated in part by Toppaladoddi and Wettlaufer [6] and Nakhla *et al.* [24], we study the effects of buoyancy and Coulomb force on the phase evolution of a pure melt by means of lattice Boltzmann numerical simulations employing an enthalpy formulation of the governing equations. The reason for our choice of the enthalpy-based method is to easily track the phase boundary by updating the total enthalpy [30] as compared with the phase-field method [31]. On the other hand, in previous studies the lattice Boltzmann method has been proved to be capable of accurately describing both the convective dynamics of solid-liquid phase change [30,32,33] and a multifield coupling problem containing the charge density, electric potential, electric field, flow field, and temperature distribution [26,27,34–38].

In the present work, we consider the effects of having a horizontal boundary at which a solid-liquid phase change occurs on Rayleigh-Bénard convection in the dielectric pure liquid, which is subjected to both temperature gradient and unipolar injection. The principle difference between the pure substance and the binary mixture is that in a binary mixture the evolving morphology affects the growth of disturbances at the mush-liquid interface through fluid flow in both the mushy layer interior and the liquid phase. However, no such mechanism exists in the pure case [6]. Specifically, we focused on (i) understanding how the melting interface and the electric field affect the Rayleigh-Bénard convection instability, and (ii) understanding how the fluid flow induced by buoyancy and/or charge injection affects the morphological instability. The present paper is organized as follows. In Sec. II we present the formulation of the physical problem. Section III is devoted to a brief presentation of the numerical method and code validation. The onset of flow motion in the presence of a melting boundary and an electric field is described in Sec. IV. We show the "locked-in" behavior of topography and how the locked-in patterns are destabilized due to the application of EHD in Sec. V. And finally in Sec. VI we present our conclusions.

II. FORMULATION OF THE PROBLEM

A. Governing equations

Consider an incompressible dielectric substance of density ρ, electrical permittivity ε, charge diffusivity D, kinematic viscosity ν, thermal diffusivity α, specific heat capacity c_p, and latent heat L_f contained between two perfectly conducting rigid horizontal planar electrodes. These two electrodes are separated by a distance of H and maintained constant though different temperatures

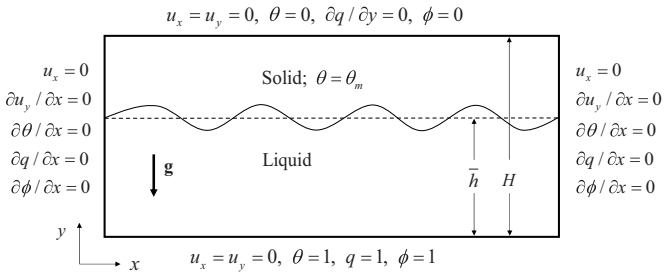

FIG. 1. Diagram of the problem and boundary conditions. The wavy line separates the solid region and liquid region. The dashed line corresponds to the average layer depth. θ_m is the melting temperature of the pure dielectric substance. The solid is isothermal so that $\theta = \theta_m$. The lower emitter electrode is the source of ions and the upper grounded electrode is the collector of ions.

and electrical potentials (see Fig. 1). The horizontal size of the electrodes is λH with λ defined as the aspect ratio. The emitter electrode at the plane $y = 0$ is held at potential $\phi = 1$ and is the source of ions which are injected into the PCM and collected by another electrode at the plane $y = H$ which is held at potential $\phi = 0$. The injection of unipolar charge of mobility K at the emitter is assumed to be "homogeneous" and "autonomous." We impose the temperature θ_h at the bottom injector and θ_c at the top collector with $\theta_c = 0 < \theta_h = 1$. The melting temperature of the PCM is such that $\theta_m = \theta_c$; this means that we focus on the particular case where the solid is isothermal.

In this paper, we consider the case of strong injection. For simplicity, we assume that permittivity and mobility are constant and equal in both phases since it has been shown that the influence of the variation in ε and K on the electrohydrodynamics is negligible under strong injection [16,17]. Also, as the residual conductivity of the substance is assumed to be very small, the currents are small enough to neglect magnetic effects as well as Joule heating in the electrohydrodynamic approximation [39]. Furthermore, we suppose that the density of the solid and the density of the liquid are equal, the solid is impenetrable, and in the liquid phase the Boussinesq approximation is applied. The resulting governing equations of this dynamical system, i.e., mechanical equations, energy equation, and electrical equations, respectively, are given as [26,35]

$$\nabla \cdot \mathbf{u} = 0, \tag{2}$$

$$\frac{\partial(\rho_0 \mathbf{u})}{\partial t} + \nabla \cdot (\rho_0 \mathbf{u}\mathbf{u}) = -\nabla \hat{p} + \nabla \cdot (\mu \nabla \mathbf{u}) + q\mathbf{E} + \rho_0 \mathbf{g}\beta(\theta - \theta_0), \tag{3}$$

$$\frac{\partial \theta}{\partial t} + \nabla \cdot (\theta \mathbf{u}) = \alpha \nabla^2 \theta - \frac{L_f}{c_p}\frac{\partial f_l}{\partial t}, \tag{4}$$

$$\nabla^2 \phi = -\frac{1}{\varepsilon} q, \tag{5}$$

$$\mathbf{E} = -\nabla \phi, \tag{6}$$

$$\frac{\partial q}{\partial t} + \nabla \cdot [(K\mathbf{E} + \mathbf{u}) \cdot q] = D\nabla^2 q. \tag{7}$$

These equations can be written in dimensionless form with the following dimensionless quantities denoted with asterisks:

$$x_i^* = \frac{x}{H}, \quad u^* = \frac{u}{\nu/H}, \quad t^* = \frac{t}{H^2/\nu}, \quad q^* = \frac{q}{q_0}, \quad \phi^* = \frac{\phi}{(\phi_0 - \phi_1)},$$
$$E_i^* = \frac{E_i}{(\phi_0 - \phi_1)/H}, \quad \theta^* = \frac{\theta}{(\theta_0 - \theta_1)}, \quad \rho^* = \frac{\rho}{\rho_0}, \quad p^* = \frac{p}{\rho_0(\nu/H)^2}. \tag{8}$$

Thus we have the set of nondimensional equations, and the asterisks are omitted for clarity:

$$\nabla \cdot \mathbf{u} = 0, \tag{9}$$

$$\frac{\partial \mathbf{u}}{\partial t} + \nabla \cdot (\mathbf{u}\mathbf{u}) = -\nabla \hat{p} + \nabla^2 \mathbf{u} + \frac{\mathrm{Ra}}{\mathrm{Pr}} \theta \mathbf{e}_z + \left(\frac{T}{M}\right)^2 qC \cdot \mathbf{E}, \tag{10}$$

$$\frac{\partial \theta}{\partial t} + \nabla \cdot (\theta \mathbf{u}) = \frac{1}{\mathrm{Pr}} \nabla^2 \theta - \frac{1}{\mathrm{St}} \frac{\partial f_l}{\partial t}, \tag{11}$$

$$\nabla^2 \phi = -Cq, \tag{12}$$

$$\mathbf{E} = -\nabla \phi, \tag{13}$$

$$\frac{\partial q}{\partial t} + \nabla \left[\left(\frac{T}{M^2} \mathbf{E} + \mathbf{u} \right) q \right] = \frac{T}{M^2} \chi \nabla^2 q, \tag{14}$$

where $\hat{p}$ and $\mathbf{e}_z$ represent the dimensionless modified pressure including the extra electrostrictive contribution and the unit vector in gravitational direction, respectively. The nondimensional parameters appearing in the equations are

$$\mathrm{Ra} = \frac{g\beta(\theta_0 - \theta_1)H^3}{\nu\alpha}, \quad \mathrm{St} = \frac{c_p(\theta_0 - \theta_1)}{L_f}, \quad \mathrm{Pr} = \frac{\nu}{\alpha},$$
$$T = \frac{\varepsilon(\phi_0 - \phi_1)}{\mu K}, \quad C = \frac{q_0 H^2}{\varepsilon(\phi_0 - \phi_1)}, \quad M = \frac{1}{K}\left(\frac{\varepsilon}{\rho_0}\right)^{1/2}, \quad \chi = \frac{D}{K(\phi_0 - \phi_1)}. \tag{15}$$

The Rayleigh number Ra and electric Rayleigh number T represent the ratio of the buoyancy and Coulomb forces to the viscous force, respectively. They are the driving parameters of the system. The Stefan number St corresponds to the ratio between specific and latent heats. The Prandtl number Pr denotes the ratio of momentum diffusivity to thermal diffusivity. The injection parameter C is the dimensionless measure of the injection level. In particular, $C \gg 1$ corresponds to the strong injection and $C \ll 1$ corresponds to the weak injection. The mobility parameter M is the ratio between the so-called hydrodynamic mobility and the true mobility of ions. χ is the dimensionless charge diffusivity coefficient. χ in conjunction with the electric Reynolds T/M^2 is known as the Schmidt number defined on the ions [40]. For typical dielectric liquids, we have $M \geqslant 3$ and $\chi = 10^{-3}$–10^{-4}.

It is useful to define the effective Rayleigh number and effective electric Rayleigh number of the fluid layer, based on the actual temperature gradient and actual potential difference across the depth of the fluid layer,

$$\mathrm{Ra}_e = \mathrm{Ra}(1 - \theta_m)\overline{h}^3 = \mathrm{Ra}\overline{h}^3, \quad T_e = T\overline{h}, \tag{16}$$

where the averaged fluid height is defined as

$$\overline{h} = \frac{1}{\lambda} \int_0^{\lambda} h(x,\ t)dx. \tag{17}$$

Here the aspect ratio λ represents the dimensionless horizontal extent. Note that in nondimensional form, we have

$$0 \leqslant \overline{h} \approx f_l \leqslant H = 1, \tag{18}$$

where f_l is the total liquid fraction and H is the dimensionless distance between the electrodes. It is easy to derive the relationship of the effective Rayleigh number and the effective electric Rayleigh

number:

$$T_e = \frac{T}{\mathrm{Ra}} \frac{\mathrm{Ra}_e}{\bar{h}^2}. \tag{19}$$

One should note that during the definition of the effective electric Rayleigh number, an implicit assumption is made that the electric potential varies linearly with the height. This is not exactly true even at the hydrostatic base state. However, according to our verification, the values of the electric potential ϕ along the height direction fall between two linear decreasing functions of the height; i.e., $\phi_1 = \phi_0(1 - \bar{h}) \leqslant \phi \leqslant \phi_2 = \phi_0(1.15 - \bar{h})$. In this study, for simplicity we use the lower bound ϕ_1 to replace the real electric potential ϕ to define the effective electric Rayleigh number. The error of this approximation is less than 15%, and in the injector and the collector this approximation is most accurate.

B. Non-Ohmic solid

According to Luo *et al.* [27], there are two typical kinds of solid, namely, the Ohmic solid and the non-Ohmic solid, distinguished by the charge-transport mechanism in the solid region. Since we consider the charge injection case here which does not obey Ohm's law, a non-Ohmic solid is considered in this study to keep consistent. In terms of the non-Ohmic solid, the charges in the solid are mainly transported by mobility under the action of the electric field [27], and since we neglect the differences of the electrical parameters between solid and liquid phase, the continuity of the electric current at the interface is straightforward.

One should note that for actual materials the ion mobility of the solid phase would be much smaller than that of the liquid phase. When considering the variation of the ion mobility between solid and liquid phase, it is reasonable to expect some different results. Nevertheless, we explore the EHD melting dynamics with the assumption of the equal electric parameters between the two phases, since the effect of these parameters on the dynamics of the convective flow have been analyzed in previous studies [26,27].

C. Boundary conditions

In this study it is assumed that the horizontal electrodes with no-slip conditions are electrically and thermally perfectly conducting. On lateral walls we adopt symmetrical boundary conditions. The associated boundary conditions on different physical fields are chosen as shown in Fig. 1. The specificity of this configuration, compared to the classical electrothermoconvection problem, lies in the Stefan conditions at the interface between solid and liquid phases. For detailed information, readers can refer to the reference therein on Rayleigh-Bénard convection with a melting boundary [7,11].

III. NUMERICAL METHOD AND VALIDATION

The set of coupled equations for velocity, temperature, charge density, and electric potential is solved with a lattice Boltzmann method, and to calculate the electric field $\mathbf{E}$, a second-order central difference scheme is applied. The details on the lattice Boltzmann method used here have already been described in Refs. [26,32,35]. To validate our LBM code, several test cases are performed and compared with the analytical solutions and available numerical benchmarks.

The electrical equations have one-dimensional electrohydrodynamic equilibrium in which fluid remains at rest. The analytical solutions in this case can be found in Ref. [41]. In Fig. 2 we plot the comparison between the analytical solution and numerical results obtained in the case of a steady hydrostatic state for various grid sizes: 100×100, 200×200, and 300×300. The numerical results from the two-relaxation-time lattice Boltzmann method (TRT LBM) [35] are also shown for comparison. A perfect agreement is found for the finest grid of 300×300. To verify the applicability of our code for solid-liquid phase transition processes, the modeling of isothermal melting of pure tin

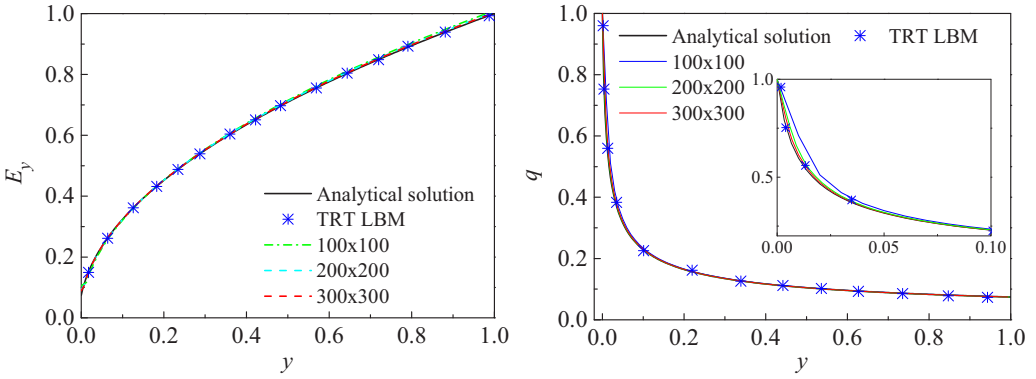

FIG. 2. Electric field (left) and charge density (right) in the steady hydrostatic state for $C = 10$. Our results with different grid sizes are compared with the analytical solutions [41] and other numerical results [36].

in a rectangular cavity is undertaken. Figure 3 gives the comparison of averaged Nusselt number and total liquid fraction between our LBM results for grid size 150×150 and Mencinger's [42] results by using the control volume method (CVM) with an adaptive grid. Also, good consistency can be seen, which demonstrates that the code we use is adequate for convective solid-liquid phase-change problems.

IV. ONSET OF FLOW MOTION

Criteria for the onset of flow motion in such a dynamical system where phase change occurs are much more complex compared to those in a single phase system, which is mainly due to the interaction between the flow and the melting boundary. In fact, for such a dynamical system, there is a timescale separation between the growth rate of the convection instability and the evolution of the background state (e.g., phase interface) [11]. This separation is dependent on the Stefan number which controls the rate of melting. In the asymptotic limit of the Stefan number tending to zero, through nonlinear asymptotic analysis, Vasil and Proctor [11] found that the onset of convection instability occurs at $\mathrm{Ra}_e = 1295.78$ for a phase-change Rayleigh-Bénard convection system. Since this regime of very small Stefan number is virtually impossible to reach numerically, most of the present numerical experiments reported that the onset of Rayleigh-Bénard convection can occur

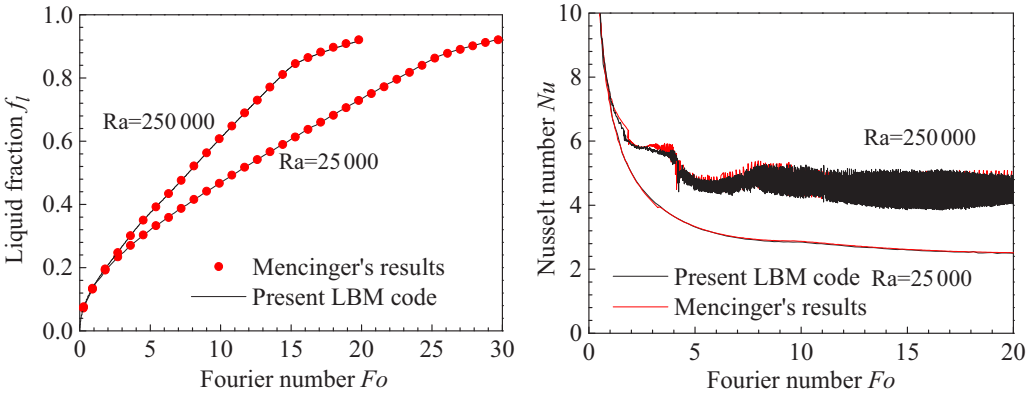

FIG. 3. Comparisons of the total liquid fraction (left) and the average Nusselt number (right) with the control volume method (CVM) with an adaptive grid [42].

at any value of effective Rayleigh number [4,7,12]. In particular, for melting with a large Stefan number which corresponds to a fast melting rate and a rapid evolution of interface, both stability analysis [12] and numerical study [4,7] have found that the Rayleigh-Bénard melting system has delayed onset events; that is, the critical Rayleigh number is larger than that in the traditional Rayleigh-Bénard system with $\mathrm{Ra}_c = 1707.76$ [43].

For the system considered in this paper which is subjected to both temperature gradient and unipolar injection, in addition to the Stefan number, the criteria of instability are also expected to be influenced by the electric Rayleigh number which plays the same important role as the Rayleigh number. It is well known that the combined effects of an electric field and a thermal gradient simultaneously applied to a horizontal dielectric liquid layer lead to the change of critical Rayleigh number, and depending on the values of Pr and M, the bifurcation of the electrothermoconvection can be subcritical or supercritical [15]. In this section, we numerically study the effects of melting boundary and electric field on the onset of flow motion. We first characterize the timescale separation of interface and convection in the absence of an electric field and study the effects of a melting boundary on the onset of Rayleigh-Bénard convection, then we analyze the characteristic timescales of the electrothermoconvection to compare the strength of the electric force and the buoyancy force, and finally we investigate the effects of electric force on the onset of flow motion in the presence of a melting interface.

A. Timescale separation

For the melting problem there is a particular timescale which is associated with the Stefan number and therefore the evolution of the interface [11]. Since the effects of interface instability on convection depend strongly on the timescale of interface evolution, it is of great importance to characterize the separation of interface timescale and that of convection. Different from the weakly nonlinear analyses which focus on the small Stefan number limit [11] or infinite Prandtl number limit [5], for now we consider an arbitrary Stefan number and Prandtl number. We start from the basic Stefan problem that the melting is one dimensional and purely governed by heat diffusion. The solution to this problem reads (here we only focus on the interface position) [44]

$$h = 2k\sqrt{\alpha t}. \tag{20}$$

Here h is the location of the phase interface, and k is related to the Stefan number and is the root of the following transcendental equation,

$$\sqrt{\pi} k e^{k^2} \mathrm{erf}(k) = \mathrm{St}, \tag{21}$$

where $\mathrm{erf}(k)$ is the error function given by

$$\mathrm{erf}(k) = \frac{2}{\sqrt{\pi}} \int_0^k e^{-\eta^2} d\eta. \tag{22}$$

We show in Fig. 4 the numerical solution of the transcendental relation for St ranging from 0 to 50. It is clear that k is a monotonically increasing function of St.

Differentiating Eq. (20) with respect to time, we obtain the interface evolution velocity for diffusion-governed melting:

$$u_i = \frac{dh}{dt} = k\sqrt{\frac{\alpha}{t}}. \tag{23}$$

From Eq. (23), it is clear that the interface evolution velocity decreases with time, and as expected u_i is an increasing function of St (note that k is an increasing function of St). Besides, the melting rate of the interface is also dependent on the thermal diffusion coefficient α, which leads to the Prandtl number dependence of timescale separation in the following. It should be noted that the above relation still remains valid for the two-dimensional or three-dimensional phase-change process before the onset of convection, in which the melting is still governed by diffusion.

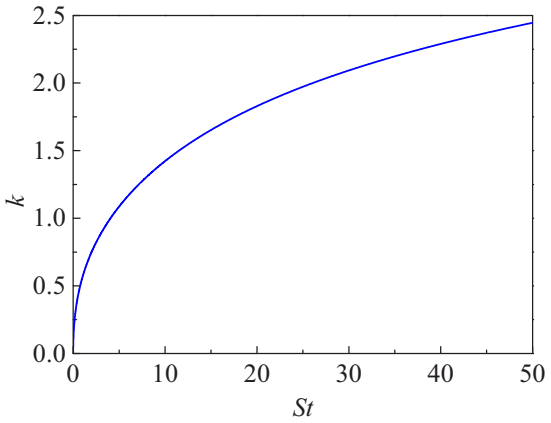

FIG. 4. The melting parameter k versus Stefan number St. Clearly, k is an increasing function of the Stefan number. Such a feature will be very important for the following analysis.

We are mainly interested in the weakly nonlinear regime near the onset of flow motion, where the melting is still controlled by diffusion, and convection is just setting in. In this situation the relation Eq. (23) remains valid. We assume that at some moment t the system is in this regime, and the height of the liquid layer (equal to the position of the interface) is h. In this sensitive regime, even a tiny perturbation from the interface, i.e., the very small evolution distance of the interface, has great influence on the convection instability. Without losing generality, we assume that this small distance is Δh. The time for interface evolution from h to $h + \Delta h$ is approximated by

$$t_i = \frac{\Delta h}{u_i} = \frac{\Delta h}{k}\sqrt{\frac{t}{\alpha}} \tag{24}$$

Corresponding to these small perturbations of the interface, the turnover time of the convection t_f is

$$t_f = \frac{h}{u_f}, \tag{25}$$

where u_f is buoyancy-driven convection velocity, defined as [45]

$$u_f = \sqrt{g\beta\Delta\theta h}. \tag{26}$$

Without losing generality, here we assume that the convection is driven by buoyancy force, and the effect of Coulomb force is neglected. Substituting the equations of buoyancy-driven convection velocity, Eq. (26), and the height of the liquid layer, Eq. (20), into the above equation, gives

$$t_f = \sqrt{\frac{2k\sqrt{\alpha t}}{g\beta\Delta\theta}}. \tag{27}$$

Now we can characterize the timescale separation between the convection and the interface by the ratio of the two timescales (the timescale of interface evolution and the timescale of convection):

$$\tau = \frac{t_i}{t_f} = \frac{\Delta h}{k}\sqrt{\frac{g\beta\Delta\theta}{\alpha}}\frac{1}{2k}\sqrt{\frac{t}{\alpha}}. \tag{28}$$

By introducing the global Rayleigh number, Eq. (15), and the Fourier number, $\mathrm{Fo} = \alpha t/H^2$, we have

$$\tau = \frac{\Delta h}{kH}\sqrt{\frac{1}{2k}\mathrm{Ra}\,\mathrm{Pr}\,\sqrt{\mathrm{Fo}}}. \tag{29}$$

The determination of Δh is interesting in its own right, although we postpone this problem to future studies. Since we only focus on the effects of dimensionless parameters on timescale separation, here we assume that the ratio $\Delta h/H$ is a constant and is substituted by γ, i.e.,

$$\tau = \frac{\gamma}{k}\sqrt{\frac{1}{2k}\mathrm{Ra}\,\mathrm{Pr}\,\sqrt{\mathrm{Fo}}}. \tag{30}$$

We could also make another choice for simplification. Introducing the effective Rayleigh number, Eq. (16), instead of the global Rayleigh number leads to

$$\tau = \frac{\gamma'}{4k^3}\sqrt{\mathrm{Ra}_e\mathrm{Pr}/\mathrm{Fo}}, \tag{31}$$

where $\gamma' = \Delta h/h$.

From Eq. (29) we find that the timescale separation of convection and interface is a function of the Rayleigh number, the Prandtl number, and the Stefan number. Since only in the weakly nonlinear regime near the onset of flow motion does this relationship remain valid, the Fourier number in Eq. (29) indeed represents the critical time when convection sets in. It is clear that the timescale separation and the critical time, as well as the critical Rayleigh number are the as yet undetermined parameters, and therefore it is difficult to solve Eq. (30) by a mathematic analysis. However, for a given Rayleigh-Bénard melting system with the set of parameters (i.e., Ra, Pr, and St) predetermined, this problem is easily solved numerically. On the other hand, since no existing theory completely accounts for the dependence of the timescale separation on Ra, Pr, and St, it is instructive to examine how the stability criteria of a Rayleigh-Bénard melting system depend on the timescale separation. And for the time being, the best method to provide insight into this problem is through numerical simulation.

B. Dependence on Stefan number and Prandtl number

In the above section we provide the derivation of the timescale separation of the dynamics of the thermal convection and that of the interface. However, the relationship between stability threshold and the timescale separation is still questionable. In this section we present systematic numerical solutions of Rayleigh-Bénard melting systems to investigate the onset of flow motion with different dimensionless parameters and therefore the timescale separations. To highlight the effects of the interface on convection instability, here the influence of the electric field is neglected. We introduce the kinetic energy density in the system to capture the onset of flow motion, which is defined by [7]

$$e_K = \frac{1}{V_f}\int_{V_f}\left(u_x^2 + u_y^2\right)dV. \tag{32}$$

Figure 5 shows the time evolution of the kinetic energy density as well as the liquid fraction versus time. Initially, the kinetic energy density of the system is very small (close to 0), and the growth rate of the liquid fraction in the first phase (represented by I in Fig. 5) is equal to the conduction melting rate. As time evolves, the system falls into zone II, as shown in Fig. 5, in which we first observe a sudden jump growth of kinetic energy density associated with the nonlinear overshoot of the instability, and simultaneously, a departure of convection melting from the conduction melting occurs. The sharp increase of kinetic energy density is followed by the decreasing fluctuation, and then the kinetic energy density tends to increase slowly with time. However, at the final stage, which corresponds to zone III in Fig. 5, we surprisingly observe a clear decrease of kinetic energy density, and the increase of the liquid fraction also slows down significantly. According to Favier *et al.*

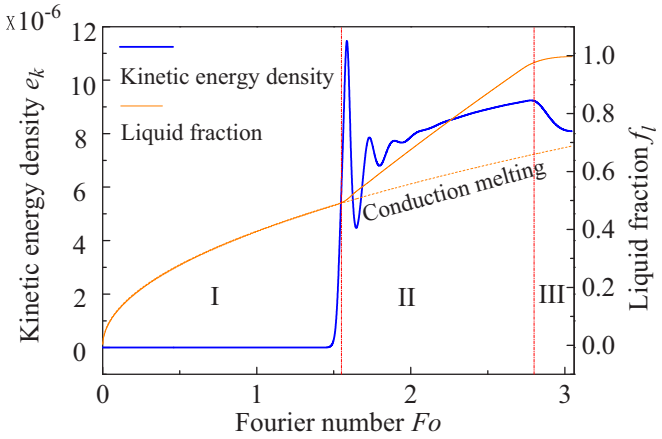

FIG. 5. The time evolution of kinetic energy density (blue solid line) and liquid fraction (orange solid line) versus time. The case of conduction melting which corresponds to the dashed orange line is also shown for comparison. The vertical dash-dotted lines, corresponding to Fo = 1.55 and 2.8, respectively, divide the figure into three zones, denoted by I, II, and III.

[7], the departure from the prediction of a purely diffusive solution marks the onset of convection. This provides a methodology to capture the critical (effective) Rayleigh number of this dynamical system, which is significantly different from what it is in traditional Rayleigh-Bénard convection without a melting top boundary [46].

Let us recall the determination of the instability threshold of buoyancy force or/and Coulomb force driven convection in a single phase [15,46]. Close to the instability threshold, the perturbations of every physical quantity f grow following an exponential law $f = f_0 e^{\sigma t}$. The growth rate σ is positive above the instability threshold and negative below it. One should note that under certain circumstances, the growth rate σ may be complex, leading to the oscillatory behavior, i.e., the overstability [47,48]. In such a dynamical system with a time-dependent interface and therefore a continuously expanding liquid layer, we believe that the long-time periodic oscillation cannot occur so that the discussion about the overstability is beyond the scope of this paper but would nevertheless prove important in other situations.

Let the system evolve from rest. For given parameters that suffice to induce motion, an interval of exponential growth will eventually appear, and one can easily determine the growth rate in this interval. Then through a linear fit of the values of σ versus driving parameters (Ra or/and T) one can obtain the instability threshold. It should be noted that before the exponential growth interval there is an initial period of latency in which the velocity is very small and varies erratically. The length of the period is related to the driving parameter, and a larger driving parameter corresponds to a shorter duration. For classical buoyancy force or/and Coulomb force driven convection, the duration of latency has no influence on the instability threshold since the set of parameters is predetermined.

When considering the presence of a melting interface, however, the situation gets more complicated. First, since the interface evolves with time, the dynamical system produces superexponential growth rather than exponential growth, which makes the traditional method described above invalid. Second, it is clear that the duration of latency strongly influences the instability threshold since the background state is time dependent, which makes it difficult to determine the intrinsic instability threshold. In this situation, a methodology based on Satbhai and Roy [8] is introduced to determine the nominal instability threshold for the dynamical system exhibiting phase transitions and convection instability. In Ref. [8] Satbhai and Roy normalized the kinetic energy density by the transient thermal diffusion speed, and the time when the normalized kinetic energy density e_k^* equals 1 marks the onset of the convection. However, according to our tests this method would be invalid

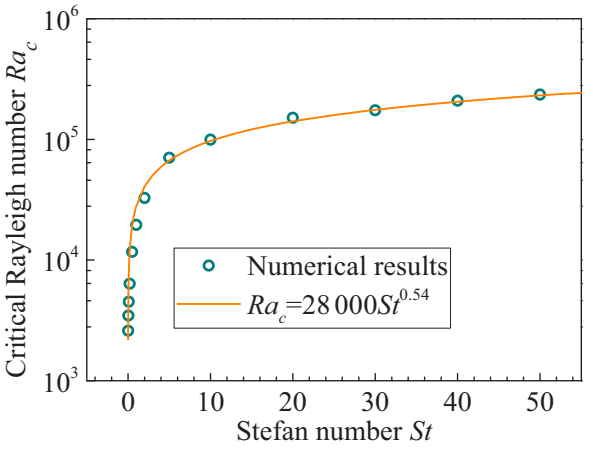

FIG. 6. Critical Rayleigh number as a function of Stefan number when $\mathrm{Ra} = 10^6$ and $\mathrm{Pr} = 1$. Circles denote the results from the numerical simulations, and the solid line represents the result from nonlinear fitting which corresponds to $\mathrm{Ra}_c = 28\,000\mathrm{St}^{0.54}$. For $\mathrm{St} = 0.02$ we obtain the smallest critical Rayleigh number of 2601.

in a wider range of combinations (Ra, Pr, St) since e_k^* would be always smaller than 1 for weakly nonlinear systems. To this end, we do not normalize e_k and use $\sqrt{e_{k\,\max} e_{k\,\min}}$ instead of 1 to mark the transition from diffusion regime to convective regime.

We first discuss the Stefan number dependence of critical Rayleigh number. In Fig. 6 we plot the critical Rayleigh number as a function of the Stefan number. The simulations are conducted with the fixed global Rayleigh number and Prandtl number ($\mathrm{Ra} = 10^6$, $\mathrm{Pr} = 1$), and the Stefan number varies from $\mathrm{St} = 2 \times 10^{-2}$ to 50. From Eq. (30), it is clear that the main consequence of increasing the Stefan number is the increase of timescale separation between the turnover time of the convective cells and the typical timescale of the topography evolution [7]. With the decrease of the Stefan number, the melting time of the interface increases due to the large amount of latent heat. In this situation, there is enough time for convection instability to grow in a quasisteady equilibrium of the interface position, and then we expect to see a clear decrease in the critical Rayleigh number, as shown in Fig. 6. In the small Stefan number limit case where $\mathrm{St} = 0.02$ which is still numerically available, the smallest critical Rayleigh number is found to be 2601, larger than the classical value of 1707.76 for traditional Rayleigh-Bénard convection [43], and larger than what it is for the weakly nonlinear regime of Vasil and Proctor [11].

Figure 7 shows the critical Rayleigh number as a function of the Prandtl number for ($\mathrm{Ra} = 10^5$, $\mathrm{St} = 0.5$). It can be seen from Eq. (30) that, contrary to the Stefan number, a high Prandtl number corresponds to large timescale separation. As a result, as shown in Fig. 7, the critical Rayleigh number tends to decrease with Prandtl number. However, there is little dependence of the critical Rayleigh number on the Prandtl number for $\mathrm{Pr} > 1$ where the critical Rayleigh number stabilizes at $\mathrm{Ra}_c = 6100$. Therefore, it is interesting to consider the solutions with a low Prandtl number. Taking the limit of a very small Prandtl number, one could obtain relatively large value of thermal diffusivity α; see Eq. (15). In this situation, the interface evolves with a relatively rapid rate so that the time interval before the melting ends is insufficient to allow the buoyancy-driven instability. As a result, the fluid still remains at rest until the critical time is reached, whereas at this stage the fluid layer has already stopped deepening, and therefore the critical Rayleigh number is expected to reach the global Rayleigh number. In Fig. 7 we show the critical Rayleigh number which is calculated based on the critical time and corresponding layer depth in Eq. (20). As expected, for $\mathrm{Pr} = 0.02$ and $\mathrm{Pr} = 0.04$ the critical Rayleigh number is larger than the given global Rayleigh number, as shown in Fig. 7.

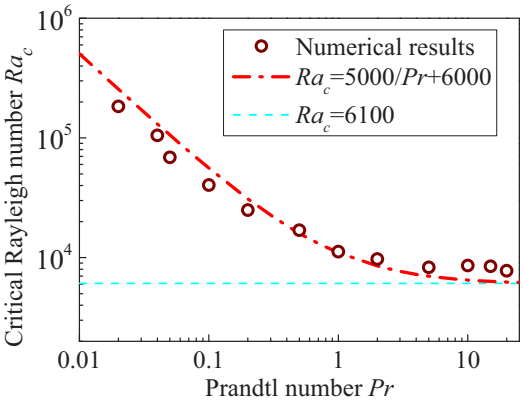

FIG. 7. The dependence of critical Rayleigh number on Prandtl number for $\mathrm{Ra} = 10^5$ and $\mathrm{St} = 0.5$. Circles correspond to the numerical simulations, and the dash-dot line corresponds to $\mathrm{Ra}_c = 5000/\mathrm{Pr} + 6000$. The critical Rayleigh numbers for $\mathrm{Pr} = 0.02$ and $\mathrm{Pr} = 0.04$ are from the critical time and corresponding layer depth in Eq. (20). For large Prandtl number we obtain the smallest critical Rayleigh number of 6100.

C. Effect of electric field

In this section, we study the effect of strong unipolar injection on the onset of Rayleigh-Bénard convection. Since this effect has been well understood in traditional electrothermoconvection systems, we mainly focus here on the dynamical system where there is a melting boundary. We start off with the analysis of different characteristic timescales since the bifurcation of electrothermoconvection is strongly dependent on thermal properties and electrical properties [15]. The relevant timescales of the problem considered here are the heat diffusion time, the viscous time, the thermal buoyancy time, the charge diffusion time, the charge drift time, and the Coulomb repulsion time [45,49]:

$$t_\nu = H^2/\nu, \quad t_\alpha = H^2/\alpha, \quad t_b = \sqrt{H/g\beta\Delta\theta}, \quad t_\chi = H^2/D, \quad t_d = H^2/K\Delta\phi, \quad t_C = \varepsilon/Kq_0. \tag{33}$$

It is easy to derive the following relationships between different timescales,

$$\begin{aligned} &t_\alpha/t_\nu = \mathrm{Pr}, \quad t_b/t_\nu = 1/\mathrm{Re}_T, \quad t_\chi/t_d = 1/\chi, \quad t_d/t_\nu = 1/\mathrm{Re}_E, \\ &t_C/t_\nu = 1/(\mathrm{Re}_E C), \quad t_C/t_d = 1/C, \end{aligned} \tag{34}$$

where Re_T and Re_E are the thermal Reynolds number and the electric Reynolds number, respectively, defined as

$$\mathrm{Re}_T = \sqrt{g\beta\Delta\theta H^3/\nu} = \sqrt{\mathrm{Ra}/\mathrm{Pr}}, \quad \mathrm{Re}_E = K\Delta\phi/\nu = T/M^2. \tag{35}$$

In this section, the following parameters are fixed: $\mathrm{Pr} = 10$, $\chi = 10^{-3}$, $C = 10$, $M = 10$, and $\mathrm{Re}_T > 1$, $\mathrm{Re}_E > 1$. In this case, the possible smallest timescale is the Coulomb repulsion time t_C or the thermal buoyancy time t_b, depending on the values of Re_T and Re_E; i.e.,

(i) when $\mathrm{Re}_T \geqslant 10\mathrm{Re}_E$, i.e., $T \leqslant \sqrt{10\mathrm{Ra}}$, the smallest timescale is t_b;
(ii) when $\mathrm{Re}_T < 10\mathrm{Re}_E$, i.e., $T > \sqrt{10\mathrm{Ra}}$, the smallest timescale is t_C.

Corresponding to the relevant timescales, there are also six velocity scales in this system (not shown). Besides, it is clear that the smallest timescale corresponds to the largest velocity scale (vice versa). In Fig. 8 we have plotted an equivalent line, the red solid diagonal, which corresponds to $T = (10\mathrm{Ra})^{0.5}$, i.e., $\mathrm{Re}_T = 10\mathrm{Re}_E$. Above this curve, we have $\mathrm{Re}_T < 10\mathrm{Re}_E$, and the electric force is larger than the buoyancy force, while below this curve we have $\mathrm{Re}_T > 10\mathrm{Re}_E$, and the electric force is smaller than the buoyancy force. One should note that for small values of Rayleigh number

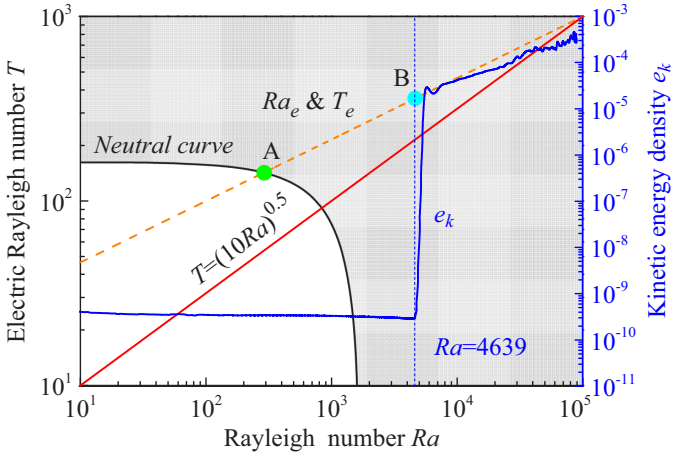

FIG. 8. The red solid curve corresponds to the equivalent line, $T = (10\mathrm{Ra})^{0.5}$, which separates the buoyancy force dominated regime and Coulomb force dominated regime. The red dashed curve shows the time evolution of effective Rayleigh number and effective electric Rayleigh number for $\mathrm{Ra} = 10^5$ and $T = 10^3$. The black solid curve corresponds to the neutral curve of traditional electrothermoconvection for $\mathrm{Pr} = 10$, $M = 10$, $C = 10$, and $\chi = 3$.

and electric Rayleigh number, the driving forces, e.g., the Coulomb force and buoyancy force, are insufficient to overcome the viscous damping and put the liquid into motion [27]. As defined in Eq. (16), the effective Rayleigh number Ra_e and the effective electric Rayleigh number T_e of the EHD melting system are the functions of the averaged height of the fluid layer which increases with time. If we choose the set of global parameters ($\mathrm{Ra} = 10^5$, $T = 10^3$) and let the system evolve from a fluid layer of zero depth, we can obtain the time evolutions of effective Rayleigh number and effective electric Rayleigh number. We show in Fig. 8 the growth of effective electric Rayleigh number versus effective Rayleigh number (see the inclined dashed line). This relationship has also been defined by Eq. (19). From Fig. 8 it is clear that during the melting process, the instantaneous Coulomb force is always larger than the instantaneous buoyancy force for a fixed layer depth.

In Fig. 8 the neutral stability curve which separates the stable and unstable regions (corresponding to the white and the gray zone, respectively) is also displayed. This neutral stability curve is predicted for the same parameters with the stability analysis approach by Rodriguez-Luis *et al.* [16], and it can also be reproduced by numerical methods [15,20,35]. For single-phase systems with dielectric liquids, this stability criterion remains, of course, valid. However, for multiphase systems, it fails. Considering the bifurcation of electroconvection with a solid-liquid interface, Luo *et al.* [27] found that the linear stability threshold is larger than that of a single-phase electroconvection problem due to the useless voltage drop at the solid phase. And for the EHD melting system considered in this study which possesses both useless voltage drop and temperature gradient at the solid phase, the stability criteria are expected to be different from the one in the single-phase problem. In addition, the dynamical effects of the melt interface on convective instability are also likely to have influence on the onset of flow motion. As discussed before, for the melting with a large Stefan number which means a fast melting, the Rayleigh-Bénard melting system usually delays the onset of flow [4,12]. When considering the coupled effects of the melting interface and unipolar injection, the numerical solution of electrothermoconvection in an EHD melting system also bears out this expectation, as shown in Fig. 8.

From Fig. 8, one observes that, starting with the initial period of latency when the kinetic energy density is very small, the dynamical EHD system bifurcates to the first interval of rapid growth, and following this period, the system enters the second interval with a smaller growth rate. It is clear

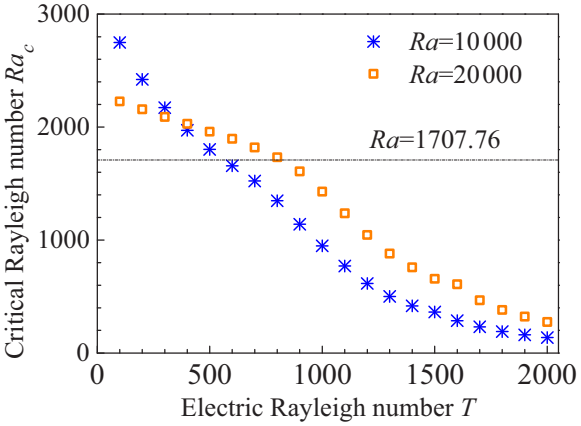

FIG. 9. Critical Rayleigh number of the fluid layer as a function of the global electric Rayleigh number for $\mathrm{Ra} = 10^4$ and $\mathrm{Ra} = 2 \times 10^4$, respectively.

that the first interval of rapid growth corresponds to the onset of convective instability. However, as shown in Fig. 8, this bifurcation of convection is far away from the neutral stability curve of the traditional electrothermoconvection as expected and, particularly, it corresponds to a larger effective Rayleigh number and effective electric Rayleigh number (see points A and B in the figure). This means that, for electrothermoconvection, the delay of onset is also a notable feature when including the presence of a melting interface.

For a more detailed analysis of unipolar injection dependence of the dynamical bifurcations of Rayleigh-Bénard convection, we restrict our attention to two specific sets of numerical simulations with $\mathrm{Ra} = 10^4$ and 2×10^4 and electric Rayleigh number T varying from 100 to 2000. The results are summarized in Fig. 9. One should note that the gravitational potential energy gradient, an important driving factor in Rayleigh-Bénard systems, is constant in both space and time [50]. And since the development of the instability is very slow at near-critical Rayleigh numbers, the computation has to be carried out for a long time before stable convection is fully developed [46]. This period of latency in which the instability is developing and the velocity is very small and varies erratically is indeed the reason why the delay of onset is one particular notable feature of Stefan-type systems. However, in the EHD case there is a highly nonlinear coupling between charge distribution and electric field in space charge transport equation [see Eqs. (6) and (7)]. Hence, the electrical potential energy gradient is no longer a constant in both space and time [50]. As shown in Fig. 9, when considering the effects of EHD in the original system, we observe that as the electric field strength increases, the critical Rayleigh number decreases significantly. For a lower Rayleigh number, which corresponds to weaker buoyancy-driven instability, we observe a much sharper decrease of convection threshold compared with the case having a higher Rayleigh number. And particularly, when the Coulomb force is strong enough so that the system enters the Coulomb force dominated regime, we see that the critical Rayleigh number is lower than the critical value 1707.76 [43] for the traditional Rayleigh-Bénard convection. Figure 10 shows the critical electric Rayleigh number as a function of the global electric Rayleigh number. As can be seen, T_c is an increasing function of T for small and moderate values of T. And interestingly, there is some dependence with the Rayleigh number, except the conditions for the large enough global electric Rayleigh numbers.

V. PATTERN FORMATION

In the above section we study the onset of flow motion in the presence of melting boundary and unipolar injection. In fact, in addition to the modification of convection instability, for the convection

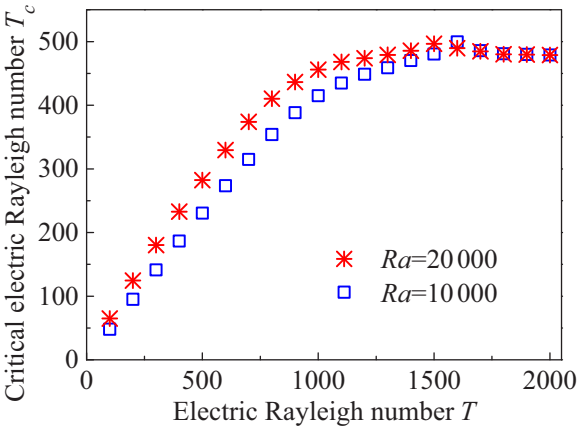

FIG. 10. Critical electric Rayleigh number of the fluid layer as a function of the global electric Rayleigh number for Ra $= 10^4$ and Ra $= 2 \times 10^4$, respectively.

with a melting top boundary there is another general feature, which is the robust locking in of spatially complex patterns [11]. In this section we present two particular numerical solutions to obtain insight into the interesting structure, and since not all possible locked-in patterns are equally stable, we will show how they are reconstructed by the electric field.

A. Locked-in behavior

First, to highlight the presence of the feedback from the Stefan condition of melting top boundary, we neglect the effect of the Coulomb force. In this case the simulation is carried out with the parameters taken as Ra $= 10^5$, Pr $= 10$, and St $= 1$. We use a reasonably large aspect ratio $\lambda = 8$ to minimize the horizontal confinement effect associated with the periodic boundary conditions [7]. The number of grids is chosen as 2400×300. We show in Fig. 11 the interface position as a function

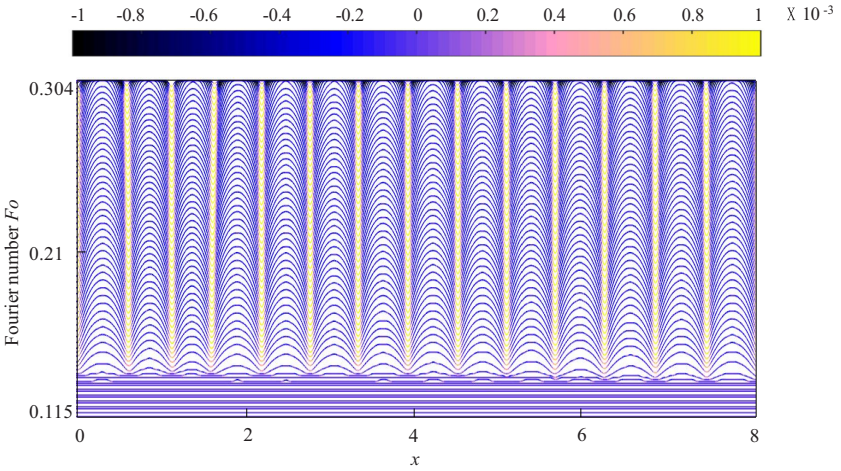

FIG. 11. A series of plots showing the time evolution of topography for Ra $= 10^5$, Pr $= 10$, and St $= 1$. The color of the curves corresponds to the curvature defined by Eq. (36). The topography begins with a planar shape in the diffusive regime, then settles into regular locked-in patterns when convection sets in, and this locked-in behavior persists until the melting ends.

of the horizontal coordinate x at different times. The color of the curves corresponds to the local signed curvature, i.e.,

$$k(x, \mathrm{Fo}) = \frac{\partial_{xx} h}{[1 + (\partial_x h)^2]^{3/2}}. \tag{36}$$

The maximum value of the curvature corresponds to cusps joining two cavities of topography and is represented by yellow.

As shown in Fig. 11, at early times when the solution is diffusive we observe the flat interface which evolves upward. As time evolves, the solution would leave the diffusive regime and enter the convective regime. Since the evolution of the topography is related to the inhomogeneous heat flux from the underlying convection rolls, we observe in the convective regime the nonplanar shape of the topography. We show in Fig. 12(a) the streamlines and isotherms at different times during the simulation. It is clearly seen that when the liquid depth reaches its critical value the convection sets in, with 28 convective cells across the whole domain. As the interface progresses, this initial set of convective rolls is vertically stretched. One particularly interesting feature of Figs. 11 and 12(a) is that the horizontal wave number of the topography is equal to that of the underlying convective rolls, and this wave number remains constant as the fluid depth increases. The long-time behavior of the wave number of the topography and the convection is surprising. Theoretically, this nonlinear equilibrium state is potentially unstable because the continuous vertical stretching of the fluid layer does not allow long-time equilibrium and the dynamical system will eventually evolve into an inherently time-dependent fashion. The work of Favier *et al.* [7] bears out this prediction whereas in our simulation we obtain different results. In fact, the long-time behavior of the wave number shown in Figs. 11 and 12(a) corresponds to the locked-in behavior [11].

According to Vasil and Proctor [11], for a long time, the dynamical Rayleigh-Bénard system grows algebraically in time, but with a locked-in spatial pattern that is determined by initial conditions. As shown in Figs. 11 and 12(a), our simulation follows the prediction of Vasil and Proctor [11]. In order to show that the locked-in behavior is a consequence of the upper boundary not being exactly planar, we perform four additional simulations with exactly the same parameters as above. The aspect ratios and the Rayleigh numbers are chosen based on the average layer depths at different times shown in Fig. 12(a). The only difference is that in the additional cases we consider the classical Rayleigh-Bénard convection which has a fixed and planar upper boundary. As shown in Fig. 12(a), with the increases of the Rayleigh number and the cavity height, the values of convective rolls decrease from 23 to 15, and the convective flow gradually loses its symmetry. This clearly shows that the locked-in pattern of the dynamical system is a consequence of the presence of the feedback of the top melting boundary, which is consistent with the conclusion of Vasil and Proctor [11].

Here we discuss the reason why in the work of Favier *et al.* [7] the dynamically evolving set of convective rolls cannot persist against the continuous vertical stretching of the fluid domain for a long time. It should be noted that for larger timescale separation the convection rolls tend to be less elongated, because the flow can quickly bifurcate to a new, more unstable set of convective rolls without any significant change in the average fluid depth [7]. Although this conclusion is drawn by reducing the Stefan number, it nevertheless remains valid when increasing the Rayleigh number to increase timescale separation due to the Rayleigh number dependence on timescale separation; see Eq. (30). In the simulation of Favier *et al.* [7] the Stefan number is identical with our simulation ($\mathrm{St} = 1$), while the Rayleigh number is chosen as $\mathrm{Ra} = 10^8$, much larger than what it is in our simulation ($\mathrm{Ra} = 10^5$). It is clear that for $\mathrm{Ra} = 10^8$ the evolution of the convection occurs on a much faster timescale than that for $\mathrm{Ra} = 10^5$. Therefore, the locked-in effects of topography on convection are weaker, and the stronger instability of convection is expected to break the locked-in patterns, resulting in the significant topography deformations. This further verifies the accuracy of the analysis of the timescale separation in the previous section.

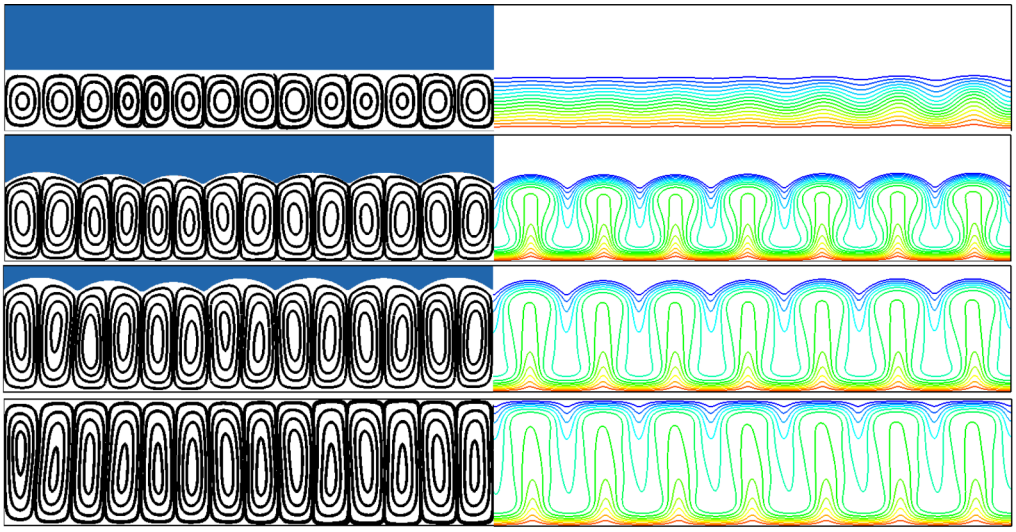

(a)

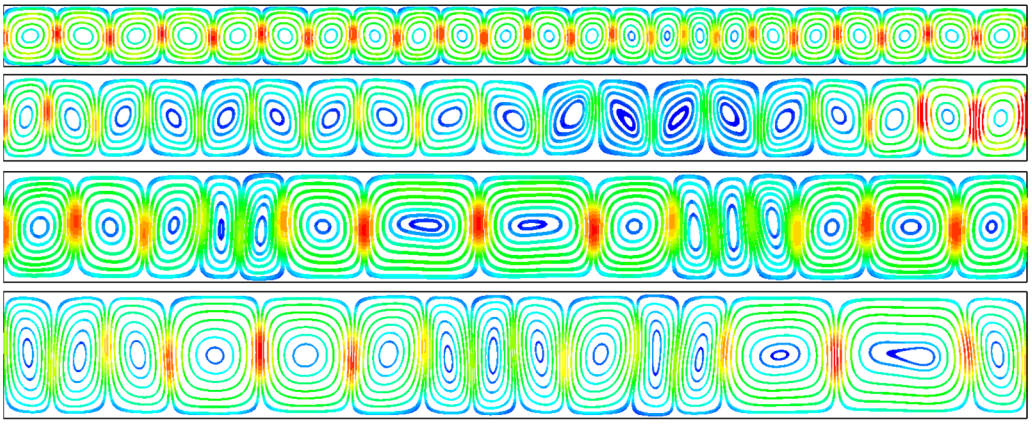

(b)

FIG. 12. (a) Visualizations of the total numerical domain for Rayleigh-Bénard melting. The streamlines are shown on the left while the isotherms are shown on the right (red and blue colors correspond to $\theta = 1$ and 0, respectively). From up to down, Fo = 1.5, 2, 2.5, 3, respectively. (b) Streamlines for classical Rayleigh-Bénard convection with aspect ratios and effective Rayleigh numbers corresponding to (a).

Figures 13(a) and 13(b) show a three-dimensional view of the spatiotemporal evolution of the fluid velocity and the spatiotemporal evolution of the temperature profile at the midheight of the fluid domain, $U(x,\ y = \overline{h}/2,\ \mathrm{Fo})$ and $\theta(x,\ y = \overline{h}/2,\ \mathrm{Fo})$, respectively. As shown in Fig. 13, at early times the solution is simply diffusive and the velocity distribution is a plane layer, which produces a uniform temperature profile; i.e.,

$$\theta(y = \overline{h}/2) \approx (T_h - T_c)/2 = 0.5. \tag{37}$$

It is interesting that after the nonlinear overshoot of the instability, we observed the decreasing fluctuation of the initial array convective rolls, which is consistent with the result shown in Fig. 5. In addition, we observe that the number of the rising hot plumes is equal to the wave number of the

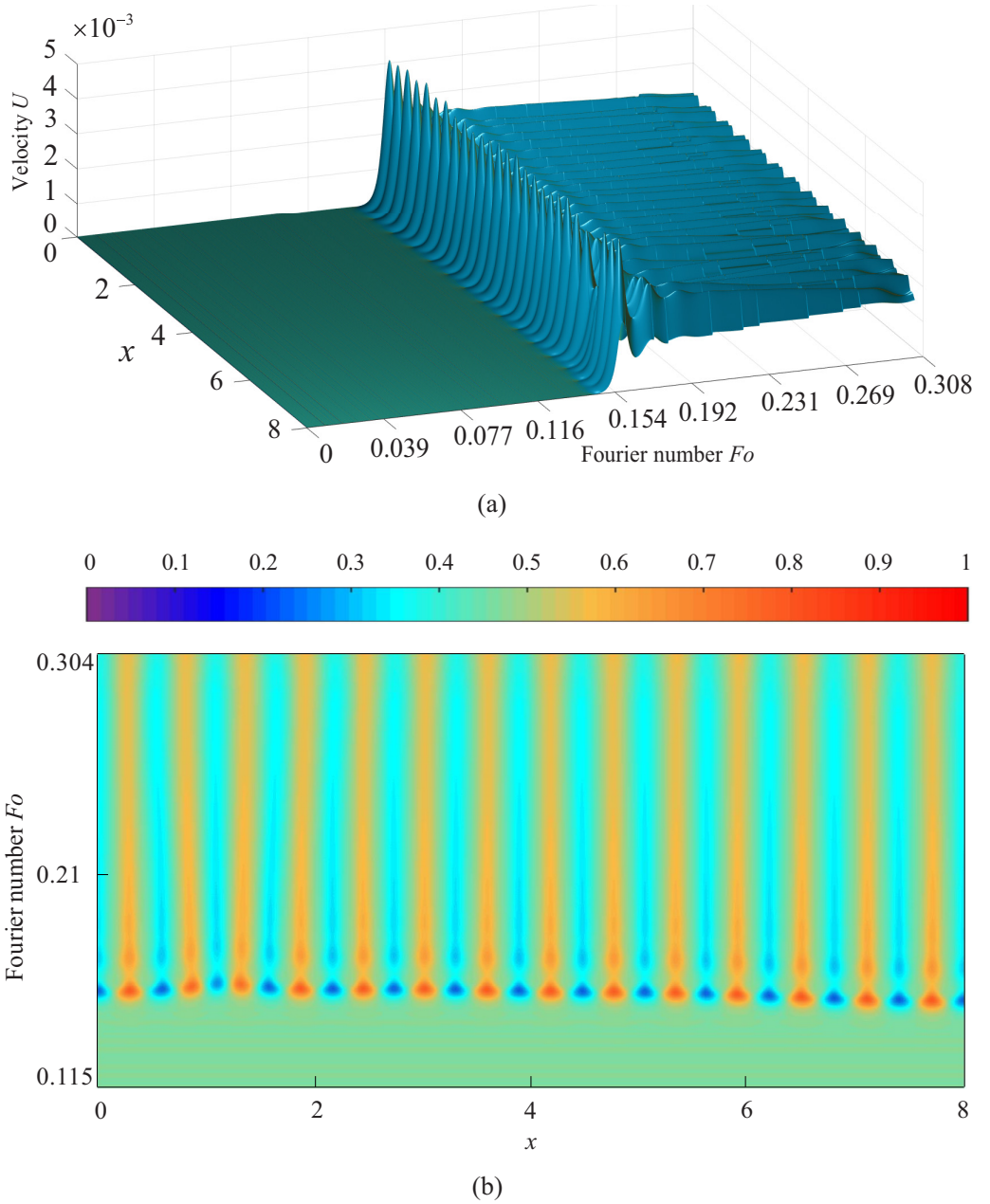

FIG. 13. (a) Three-dimensional view of the spatiotemporal evolution of the fluid velocity. (b) Spatiotemporal evolution of the temperature at the middle of the fluid layer for Ra $= 10^5$, Pr $= 10$, and St $= 1$. The dark blue color represents $\theta = 0$ while the bright red color represents $\theta = 1$. Time increases from bottom to top.

topography, which is a reflection of the impingement of the convective rolls on the interface that drive the intense localized melting events with large melting rates. Since the system evolves with a locked-in spatial pattern, as time evolves the thermal rising plumes and cold sinking plumes are extremely stable and do not seem to move horizontally as they did in Ref. [7].

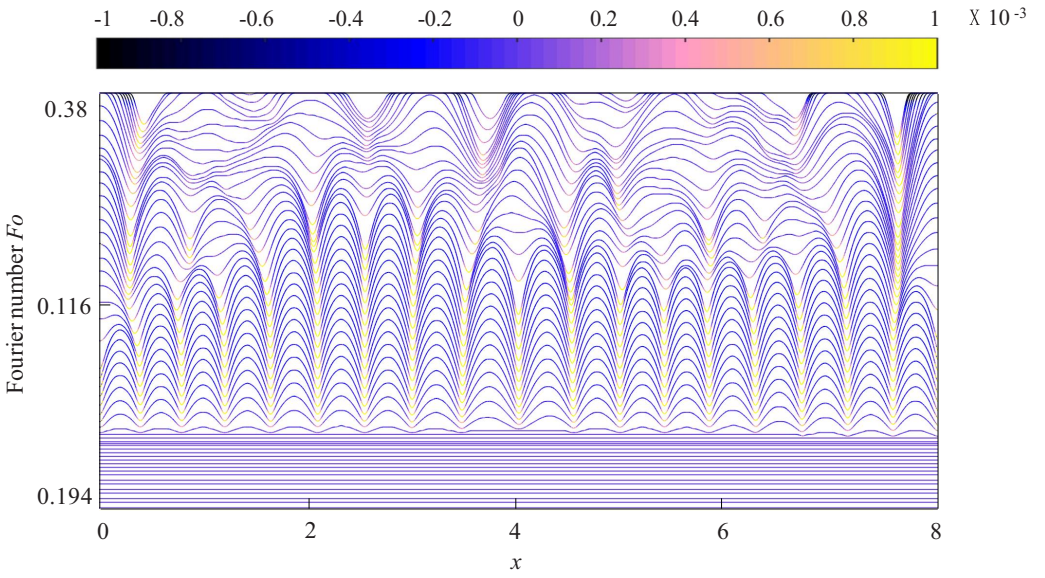

FIG. 14. A series of plots showing the time evolution of topography for $\mathrm{Ra} = 10^5$, $\mathrm{Pr} = 10$, $\mathrm{St} = 1$, $T = 10^3$, $C = 10$, $M = 10$, and $\chi = 10^{-3}$. The topography begins with the planar shape in the diffusive regime, then settles into regular locked-in patterns when convection sets in, and eventually loses its symmetry due to the presence of Coulomb force.

B. Second bifurcation under EHD

For now, we know that our system contains the potential to produce self-similarly growing locked-in patterns. For moderate Rayleigh numbers (e.g., $\mathrm{Ra} = 10^5$), due to the strong locked-in effects (stabilization) of the topography, the wavelength of the topography and convection rolls remains identical and constant; for large Rayleigh numbers, however, the dynamical system is expected to exhibit inevitable transitions between steady, periodic, and chaotic solutions [7]. This section's goal is to examine the second bifurcation of convection for a moderate Rayleigh number in the presence of an electric field which destabilizes the initial set of convection rolls. We show this type of behavior in Figs. 14 and 15 with similar thermophysical parameters as considered in the previous case but having electrical parameters of $T = 10^3$, $M = 10$, $C = 10$, and $\chi = 10^{-3}$. We also choose $\lambda = 8$ and the number of grids of 2400×300 in this simulation. This solution is somewhat similar to that with consideration of the large Rayleigh number dynamical system by Favier *et al.* [7]. In Fig. 14 we clearly see the three different regimes in the simulation: The first two share a strong analogy with the case described in Sec. V A, while the last one exhibits more complex time-dependent dynamics.

The successive bifurcations between different roll sizes is clearly visible for large layer depth. As shown in Figs. 14 and 15, at early times when Ra_e and T_e are relative small, the stabilizing effect that the topography exerts on the flow leads to the locked-in patterns which are similar to those for the previous case with no EHD (see Fig. 13), but the wave number of the former is larger. As time evolves, the nonlinear saturation of the secondary convection instability leads to the second bifurcation which corresponds to the merging of thermal rising plumes. The detailed nature of the second bifurcation is associated with the horizontally averaged mean flow, which has been qualitatively understood by Favier *et al.* [7]. As shown in Fig. 15(b), the second bifurcation corresponds to the merging of thermal rising plumes, and once the initial set of rolls is disrupted by the horizontal mean flow, a new set of convection rolls sets in, which has a larger horizontal wavelength; see Figs. 14 and Fig. 15(a). Since the buoyancy and Coulomb forces keep increasing

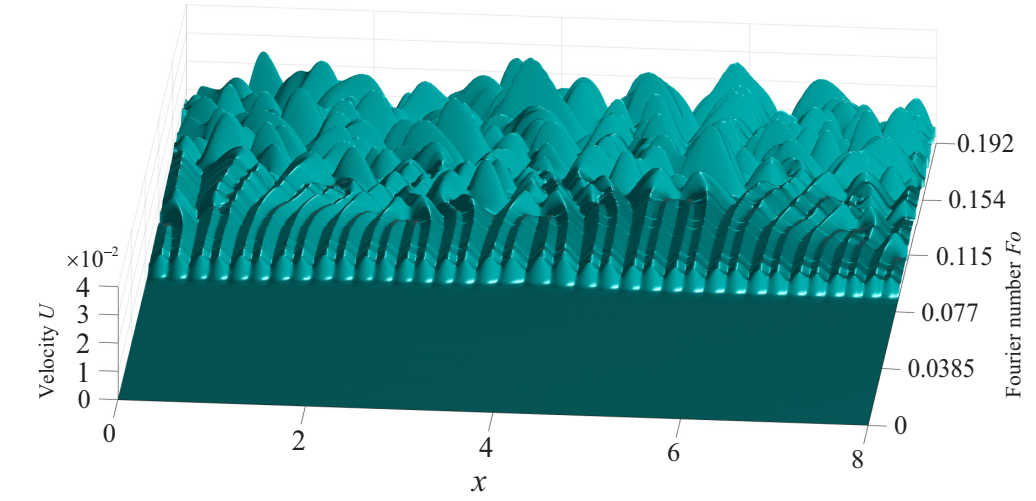

(a)

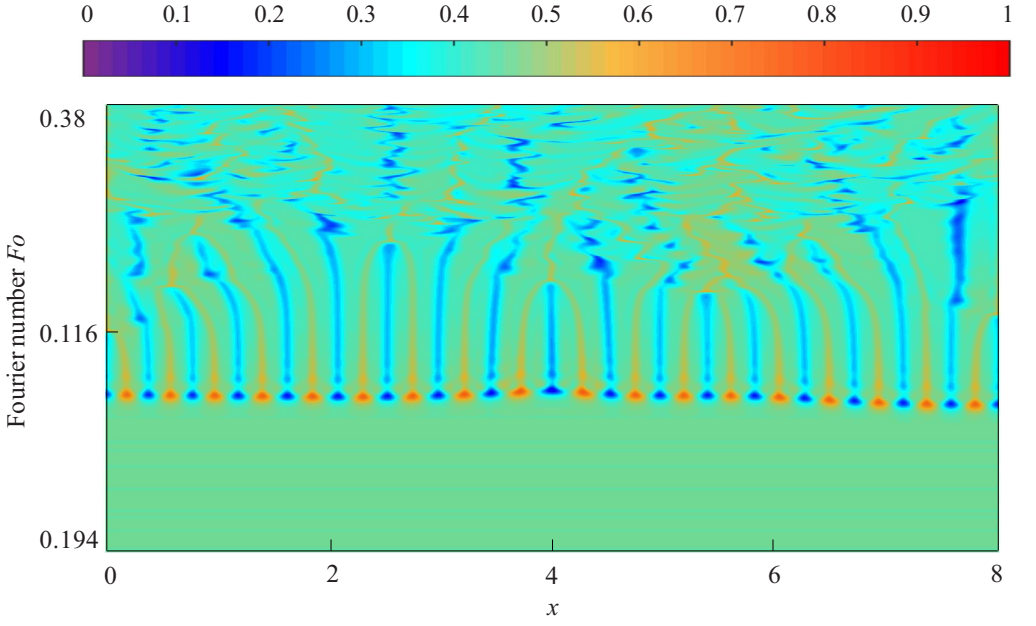

(b)

FIG. 15. (a) Three-dimensional view of the spatiotemporal evolution of the fluid velocity. (b) Spatiotemporal evolution of the temperature at the middle of the fluid layer for Ra $= 10^5$, Pr $= 10$, St $= 1$, $T = 10^3$, $C = 10$, $M = 10$, and $\chi = 10^{-3}$. The dark blue color represents $q = 0$ while the bright red color represents $q = 10$. Time increases from bottom to top.

with time, this destabilization of convection rolls is expected to repeat itself and one might expect its dynamic behavior to become more and more complex, transiting from stable to periodic and eventually chaotic solutions.

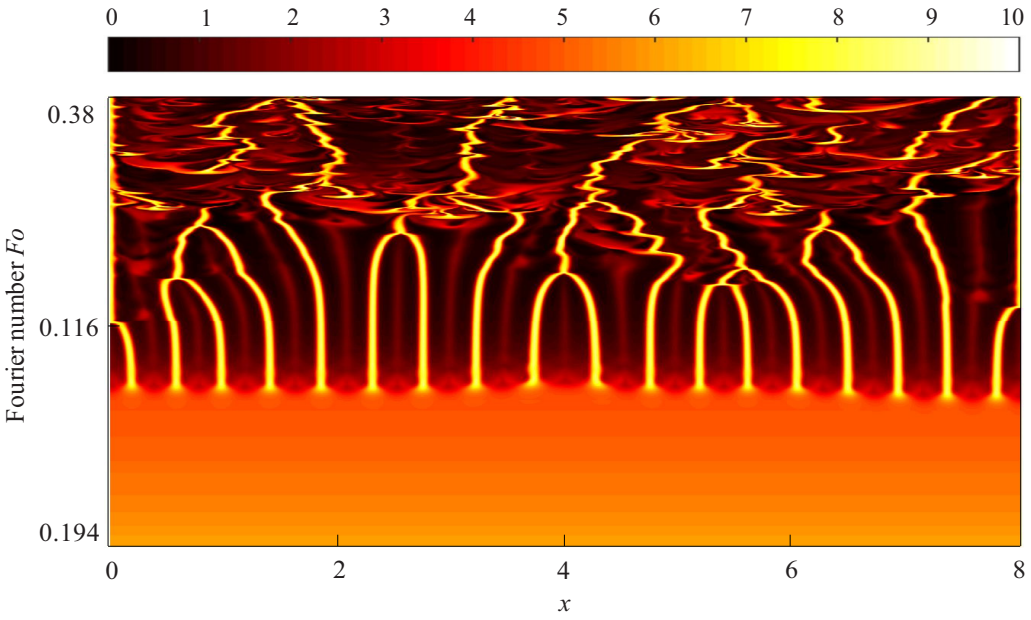

FIG. 16. Spatiotemporal evolution of the charge density at the middle of the fluid layer for $\mathrm{Ra} = 10^5$, $\mathrm{Pr} = 10$, $\mathrm{St} = 1$, $T = 10^3$, $C = 10$, $M = 10$, and $\chi = 10^{-3}$. The black color represents $q = 0$ while the bright golden color represents $q = 10$. Time increases from bottom to top.

Here we discuss the underlying mechanism responsible for the complicated behaviors in the EHD case shown in this section. As shown in Fig. 8, the instantaneous Coulomb force is always larger than the instantaneous buoyancy force for given parameters. It is therefore believed that the complicated behaviors of neighbor cells merging are due to the Coulomb force. This is indeed possible since the complex electroconvective instability arises when the effective electric Rayleigh number exceeds a certain stability threshold [51], and when considering the strong unipolar charge injection, it is found that Rayleigh-Bénard secondary instability tends to be suppressed by EHD [52]. In detail, for electroconvection in a cavity having an aspect ratio of 0.614 with the free boundary conditions for lateral walls, at $T = 213$ ($M = 10, C = 10$) Hopf bifurcation occurs and the one-cell convective flow tends to oscillate; then at $T = 281$ the convection bifurcates into a two-cell symmetric steady state. If T is increased to $T = 419$ the reflection symmetry of the two-cell convection will be broken by another Hopf bifurcation; furthermore, if T keeps increasing the chaotic convection becomes present [51]. In comparison, classical Rayleigh-Bénard convection (with an aspect ratio of 2) does not show the self-sustained periodic oscillation until the Rayleigh number reaches $\mathrm{Ra} = 10^5$ for $\mathrm{Pr} = 10$ [52], and one should note that the present dynamical system is limited to $\mathrm{Ra}_e < 10^5$ during simulation. According to Li *et al.* [52], when strong unipolar injection from below is applied, the secondary instability of Rayleigh-Bénard convection can be inhibited if the electric Rayleigh number is smaller than 1000. In our simulation, the inevitable transitions between steady and chaotic solution are clearly observed but just delayed by the presence of the topography. Compared with the classical electrothermoconvection, the transitions reappear at much larger effective Rayleigh numbers and effective electric Rayleigh numbers. Therefore, it is believed that the more and more complex dynamics is not so much a consequence of the increasing buoyancy, but rather of the presence of the electroconvective instability.

Finally, it is interesting to consider the spatiotemporal evolution of charge density which is shown in Fig. 16. Before that, one should note that charge density may change via three mechanisms: drift under the action of electric field, convection by the velocity field of the fluid, and charge

diffusion [53]. Although it is common practice to neglect the charge diffusion due to the smallness of the coefficient, we nevertheless consider this term in our simulation to keep the nature of the charge conservation equation from a second-order elliptic partial-differential equation to a first-order hyperbolic one [53]. As seen in Fig. 16, electroplumes are generated when convection rolls set in, and with the appearance of unsteady convection, the distribution of charge density presents chaotic characteristics, dependent on time and space. In addition to charged plumes, we also observe in Fig. 16 that some certain regions cannot be reached by the ions, and hence are void of charge. This is due to the fact that when Coulomb-driven convection sets in, it always takes place with a maximum velocity greater than the ion drift velocity and therefore a region develops where ions cannot enter [54]. The structure of the charge density contours with the region void of charge is a characteristic feature of EHD problems, and many previous numerical simulations have predicted this behavior [20,26,28,35].

VI. CONCLUSIONS

We have studied the influence of melting boundary and electric field on the onset and pattern formation of Rayleigh-Bénard convection. Starting with the one-dimensional Stefan problem, we have derived the equations that characterize the timescale separation between the turnover time of the convective cells and the typical timescale of evolution of the topography. This separation is dependent on the inherent dimensionless parameters of convective melting, i.e., Ra, Pr, and St. By decreasing the Stefan number or increasing the Prandtl number to compare the dependence of the onset of convection on separation, we found that the critical Rayleigh number is a decreasing function of timescale separation. In the case of EHD melting, the onset of flow motion would be advanced when increasing the electric field and, particularly, the critical Rayleigh number can be smaller than the classical value ($\mathrm{Ra}_c = 1707.76$) for traditional Rayleigh-Bénard convection [43] if the electric field is strong enough.

For $\mathrm{Ra} = 10^5$, $\mathrm{Pr} = 10$, and $\mathrm{St} = 1$, we have predicted the locked-in spatial pattern which was derived by Vasil and Proctor through weakly nonlinear analysis [11]. Due to the locked-in effects that topography imprints on convection, the wave number of the topography and the underlying convection remain identical and constant for a long time once the flow motion sets in. However, this locked-in pattern would be broken down when there is a strong enough electric field across the domain inducing the strong electroconvective instability to destabilize the system. Finally, we have shown the spatiotemporal evolution of charge density in the EHD case, in which we observed interesting phenomena associated with the competition of the three different kinds of charge-transport mechanisms.

ACKNOWLEDGMENTS

This work is supported by the National Natural Science Foundation of China (Grants No. 51906051 and No. 52076055), the Fundamental Research Funds for the Central Universities (Grant No. AUGA5710094020), and Anhui Provincial Natural Science Foundation (Grant No. 1908085MF208).

[1] J. Pedlosky, *Geophysical Fluid Dynamics*, 2nd ed. (Springer, Berlin, 1987).

[2] V. Solomatov, *Treatise on Geophysics*, 2nd ed., edited by G. Schubert (Elsevier, Oxford, UK, 2015), pp. 87–104.

[3] C. Polashenski, K. M. Golden, D. K. Perovich, E. Skyllingstad, A. Arnsten, C. Stwertka, and N. Wright, Percolation blockage: A process that enables melt pond formation on first year arctic sea ice, J. Geophys. Res.: Oceans **122**, 413 (2017).

[4] B. R. Esfahani, S. C. Hirata, S. Berti, and E. Calzavarini, Basal melting driven by turbulent thermal convection, Phys. Rev. Fluids **3**, 053501 (2018).
[5] S. Labrosse, A. Morison, R. Deguen, and T. Alboussière, Rayleigh-Bénard convection in a creeping solid with melting and freezing at either or both its horizontal boundaries, J. Fluid Mech. **846**, 5 (2018).
[6] S. Toppaladoddi and J. S. Wettlaufer, The combined effects of shear and buoyancy on phase boundary stability, J. Fluid Mech. **868**, 648 (2019).
[7] B. Favier, J. Purseed, and L. Duchemin, Rayleigh-Benard convection with a melting boundary, J. Fluid Mech. **858**, 437 (2019).
[8] O. Satbhai and S. Roy, Criteria for the onset of convection in the phase-change Rayleigh-Bénard convection system with moving melting-boundary, Phys. Fluids **32**, 064107 (2020).
[9] S. H. Davis, U. Müller, and C. Dietsche, Pattern selection in single-component systems coupling Bénard convection and solidification, J. Fluid Mech. **144**, 133 (1984).
[10] M. Sugawara, E. Tamura, Y. Satoh, Y. Komatsu, M. Tago, and H. Beer, Visual observations of flow structure and melting front morphology in horizontal ice plate melting from above into a mixture, Heat Mass Transfer **43**, 1009 (2006).
[11] G. M. Vasil and M. R. E. Proctor, Dynamic bifurcations and pattern formation in melting-boundary convection, J. Fluid Mech. **686**, 77 (2011).
[12] M. C. Kim, D. W. Lee, and C. K. Choi, Onset of buoyancy-driven convection in melting from below, Korean J. Chem. Eng. **25**, 1239 (2008).
[13] G. Venezian, Effect of modulation on the onset of thermal convection, J. Fluid Mech. **35**, 243 (1969).
[14] J. M. Aurnou and P. L. Olson, Experiments on Rayleigh-Bénard convection, magnetoconvection and rotating magnetoconvection in liquid gallium, J. Fluid Mech. **430**, 283 (2001).
[15] P. H. Traoré, A. T. Pérez, D. Koulova, and H. Romat, Numerical modelling of finite-amplitude electro-thermo-convection in a dielectric liquid layer subjected to both unipolar injection and temperature gradient, J. Fluid Mech. **658**, 279 (2010).
[16] A. Rodriguez-Luis, A. Castellanos, and A. T. Richardson, Stationary instabilities in a dielectric liquid layer subjected to an arbitrary unipolar injection and adverse thermal gradient, J. Phys. D: Appl. Phys. **19**, 2115 (1986).
[17] P. Atten, F. M. J. McCluskey, and A. T. Pérez, Electroconvection and its effect on heat transfer, IEEE Trans. Electr. Insul. **23**, 659 (1988).
[18] F. M. G. McCluskey, P. Atten, and A. T. Pérez, Heat transfer enhancement by electroconvection resulting from an injected space charge between parallel plates, Int. J. Heat Mass Transfer **34**, 2237 (1991).
[19] Y. F. Guan, J. Riley, and I. Novosselov, Three-dimensional electroconvective vortices in cross flow, Phys. Rev. E **101**, 033103 (2020).
[20] J. Wu and P. Traoré, A finite-volume method for electro-thermo-convective phenomena in a plane layer of dielectric liquid, Numer. Heat Transfer, Part A **68**, 471 (2015).
[21] S. Laohalertdecha, P. Naphon, and S. Wongwises, A review of electrohydrodynamic enhancement of heat transfer, Renewable Sustainable Energy Rev. **11**, 858 (2007).
[22] S. Rashidi, H. Bafekr, R. Masoodi, and E. M. Languri, EHD in thermal energy systems—a review of the applications, modelling, and experiments, J. Electrostat. **90**, 1 (2017).
[23] D. Nakhla, H. Sadek, and J. S. Cotton, Melting performance enhancement in latent heat storage module using solid extraction electrohydrodynamics (EHD), Int. J. Heat Mass Transfer **81**, 695 (2015).
[24] D. Nakhla, E. Thompson, B. Lacroix, and J. S. Cotton, Measurement of heat transfer enhancement in melting of n-Octadecane under gravitational and electrohydrodynamics (EHD) forces, J. Electrost. **92**, 31 (2018).
[25] B. T. Chu, Thermodynamics of electrically conducting fluids, Phys. Fluids **2**, 473 (1959).
[26] K. Luo, A. T. Pérez, J. Wu, H. L. Yi, and H. P. Tan, Efficient lattice Boltzmann method for electrohydrodynamic solid-liquid phase change, Phys. Rev. E **100**, 013306 (2019).
[27] K. Luo, J. Wu, A. T. Pérez, H. L. Yi, and H. P. Tan, Stability analysis of electroconvection with a solid-liquid interface via the lattice Boltzmann method, Phys. Rev. Fluids **4**, 083702 (2019).
[28] K. He, Z. H. Chai, L. Wang, B. Ma, and B. C. Shi, Numerical investigation of electro-thermo-convection with a solid-liquid interface via the lattice Boltzmann method, Phys. Fluids **33**, 037128 (2021).

[29] L. Ristroph, Sculpting with flow, J. Fluid Mech. **838**, 1 (2018).
[30] S. Chakraborty and D. Chatterjee, An enthalpy-based hybrid lattice-Boltzmann method for modelling solid-liquid phase transition in the presence of convective transport, J. Fluid Mech. **592**, 155 (2007).
[31] C. Beckermann, H.-J. Diepers, I. Steinbach, A. Karma, and X. Tong, Modelling melt convection in phase-field simulations of solidification, J. Comput. Phys. **154**, 468 (1999).
[32] R. Z. Huang, H. Y. Wu, and P. Chen, A new lattice Boltzmann model for solid-liquid phase change, Int. J. Heat Mass Transfer **59**, 295 (2013).
[33] Q. Liu, Y. L. He, and Q. Li, Enthalpy-based multi-relaxation-time lattice Boltzmann method for solid-liquid phase-change heat transfer in metal foams, Phys. Rev. E **96**, 023303 (2017).
[34] K. Luo, J. Wu, H. L. Yi, and H. P. Tan, Lattice Boltzmann model for Coulomb-driven flows in dielectric liquids, Phys. Rev. E **93**, 023309 (2016).
[35] K. Luo, J. Wu, H. L. Yi, and H. P. Tan, Lattice Boltzmann modelling of electro-thermo-convection in a planar layer of dielectric liquid subjected to unipolar injection and thermal gradient, Int. J. Heat Mass Transfer **103**, 832 (2016).
[36] Y. F. Guan and I. Novosselov, Two relaxation time lattice Boltzmann method coupled to fast Fourier transform Poisson solver: Application to electroconvective flow, J. Comput. Phys. **397**, 108830 (2019).
[37] Y. F. Guan and I. Novosselov, Numerical analysis of electroconvection in cross-flow with unipolar injection, Phys. Rev. Fluids **4**, 103701 (2019).
[38] B. J. Zhu, Y. F. Guan, and J. Wu, Two-relaxation time lattice Boltzmann models for the ion transport equation in electrohydrodynamic flow: D2Q5 vs D2Q9 and D3Q7 vs D3Q27, Phys. Fluids **33**, 044108 (2021).
[39] J. R. Melcher, *Continuum Electromechanics* (The MIT Press, Cambridge, MA, 1981).
[40] Y. F. Guan, T. H. Yang, and J. Wu, Mixing and transport enhancement in microchannels by electrokinetic flows with charged surface heterogeneity, Phys. Fluids **33**, 042006 (2021).
[41] M. Zhang, F. Martinelli, J. Wu, P. J. Schmid, and M. Quadrio, Modal and non-modal stability analysis of electrohydrodynamic flow with and without cross-flow, J. Fluid Mech. **770**, 319 (2015).
[42] J. Mencinger, Numerical simulation of melting in two-dimensional cavity using adaptive grid, J. Comput. Phys. **198**, 243 (2004).
[43] S. Chandrasekhar, *Hydrodynamic and Hydromagnetic Stability* (Dover, New York, 1961).
[44] A. Solomon, Some remarks on the Stefan problem, Math. Comput. **20**, 347 (1966).
[45] K. Luo, J. Wu, H. L. Yi, and H. P. Tan, Numerical investigation of heat transfer enhancement in electro-thermo-convection in a square enclosure with an inner circular cylinder, Int. J. Heat Mass Transfer **113**, 1070 (2017).
[46] X. Shan, Simulation of Rayleigh-Bénard convection using a lattice Boltzmann method, Phys. Rev. E **55**, 2780 (1997).
[47] Y. F. Guan, X. R. He, Q. Wang, Z. W. Song, M. Q. Zhang, and J. Wu, Monotonic instability and overstability in two-dimensional electrothermohydrodynamic flow, Phys. Rev. Fluids **6**, 013702 (2021).
[48] A. N. Mordvinov and B. L. Smorodin, Electroconvection under injection from cathode and heat from above, J. Exp. Theor. Phys. **114**, 870 (2012).
[49] P. A. Vázquez, G. E. Georghiou, and A. Castellanos, Numerical analysis of the stability of electroconvection between two plates, J. Phys. D: Appl. Phys. **41**, 175303 (2008).
[50] A. Kourmatzis and J. S. Shrimpton, Turbulent three-dimensional dielectric electrodynamic convection between two plates, J. Fluid Mech. **696**, 228 (2012).
[51] B. F. Wang and T. W. H. Sheu, Numerical investigation of electrohydrodynamic instability and bifurcation in a dielectric liquid subjected to unipolar injection, Comput. Fluids. **136**, 1 (2016).
[52] T. F. Li, K. Luo, and H. L. Yi, Suppression of Rayleigh-Bénard secondary instability in dielectric fluids by unipolar charge injection, Phys. Fluids **31**, 064106 (2019).
[53] A. T. Pérez and A. Castellanos, Role of charge diffusion in finite-amplitude electroconvection, Phys. Rev. A **40**, 5844 (1989).
[54] A. Castellanos and P. Atten, Numerical modeling of finite amplitude convection of liquids subjected to unipolar injection, IEEE Trans. Ind. Appl. **IA-23**, 825 (1987).